Sustainable
Energy & Fuels

ROYAL SOCIETY
OF CHEMISTRY

PAPER

View Article Online
View Journal | View Issue

Published on 27 June 2022. Downloaded by State University of New York at Stony Brook on 7/17/2023 12:32:59 PM.

Check for updates

Cite this: *Sustainable Energy Fuels*, 2022, **6**, 3669

Nitro-oxidized carboxylated cellulose nanofiber based nanopapers and their PEM fuel cell performance†

Sunil K. Sharma,*[a] Priyanka R. Sharma,[a] Likun Wang,[b] Micheal Pagel,[c] William Borges,[a] Ken I. Johnson,[a] Aniket Raut,[b] Kevin Gu,[a] Chulsung Bae,[c] Miriam Rafailovich*[b] and Benjamin S. Hsiao*[a]

Received 29th March 2022
Accepted 26th June 2022

DOI: 10.1039/d2se00442a

rsc.li/sustainable-energy

The fuel cell is the best alternative to compensate for today's energy demand, but the high cost of fabrication of membranes (*e.g.*, Nafion) hampers the widespread commercialization. Plant-derived nanocellulose is renewable, most abundant, and biocompatible with high strength and tunable surface chemistry. Here we have demonstrated the jute derived-nitro-oxidized carboxycellulose nanofibers (NOCNFs) as a viable and sustainable substitute for synthetic ionomer membranes used in proton exchange fuel cells (PEFCs). NOCNFs were obtained in two functionalities: carboxylate and carboxylic acid which were then transformed into nanopaper I and II, respectively. This is the first report where NOCNFs with two different functionalities were tested in PEFCs. The results indicated that nanopaper II performed better than nanopaper I with a high proton conductivity of 14.2 mS cm^{-1} and power density of 19.1 mW cm^{-2} at high temperature (80 °C) operation in PEFCs, along with excellent durability even for 24 h of operation.

Introduction

The global population is projected to reach 9.7 billion by 2050, and with this, the global electricity demand is expected to grow by 150% to 53.6 billion MW h.[1] In order to sustainably meet this demand, improved energy efficient and renewable energy sources are needed. In this regard, hydrogen fuel cell technologies present an attractive energy carrying solution due to their flexibility, clean emissions, and efficiency.[2–8]

Proton exchange membrane fuel cells (PEMFCs) are electrochemical devices that catalyze the spontaneous redox reaction between $H_{2(g)}$ and $O_{2(g)}$ to create a potential difference between electrodes.[9] Thus, energy from an intermittent source can be converted and used on demand from a gas-based storage. In particular, the only commercial proton exchange membrane used is Nafion, a fluoropolymer that conducts protons *via* sulfonic acid groups.[10,11] Unfortunately, the limitations associated with Nafion include: (i) high cost *i.e.* ∼US\$ 800 per m^2,[12] (ii) susceptibility to hydrogen gas crossover,[13] (iii) complex recycling process,[14] (iv) non-biodegradability and (v) loss of performance (proton conductivity and mechanical stability) at low relative humidity (RH) and high temperature.[15] Therefore, an inexpensive, greener, and more stable membrane is imperative to increase the viability of PEMFCs on a large scale.

Plant-based nanocellulose is the most abundant, inexpensive and renewable nanomaterial that has potential in many different applications including pharmaceuticals,[16] food,[17] energy storage,[18] water purification,[19] biomedicine,[20] 3D printing and tissue engineering.[21] Functionalized nanocellulose is one of the most anticipated alternative membrane precursors with several groundbreaking properties due to the presence of abundant hydroxyl groups available for chemical modifications or hydrogen bonding networks.[22–26] Mainly, there are two forms of plant derived nanocelluloses: cellulose nanocrystals (CNCs) and cellulose nanofibrils (CNFs).[27] CNCs are cellulose crystals with a width of about 10 nm and a length of several hundred nanometers; they are made by strong acid hydrolysis of cellulose which removes hydrolyzed noncrystalline regions more easily.[28] However, CNFs have varying morphologies compared to CNCs; they are mostly produced by TEMPO oxidation,[29–31] carboxymethylation,[32] phosphorylation,[33] acetylation,[34] silylation,[35] and nitro-oxidation[25,27] of cellulose. Most of the above processes generate CNFs with negative surface charges which not only facilitate nanofiber dispersion in suspensions, but also provide functional sites for utilization in various applications

---

[a] *Department of Chemistry, Stony Brook University, Stony Brook, New York, 11794, USA. E-mail: sunil.k.sharma@stonybrook.edu; benjamin.hsiao@stonybrook.edu; Tel: +16314282528; +16316327793*

[b] *Department of Material Science and Chemical Engineering, Stony Brook University, Stony Brook, New York, 11794, USA. E-mail: miriam.rafailovich@stonybrook.edu; Tel: +15164589011*

[c] *Department of Chemistry and Chemical Biology, Rensselaer Polytechnic Institute, Troy, New York, 12180, USA*

† Electronic supplementary information (ESI) available. See **https://doi.org/10.1039/d2se00442a**

Published on 27 June 2022. Downloaded by State University of New York at Stony Brook on 7/17/2023 12:32:59 PM.

including adsorption, sensing, catalysis and for further chemical modification.[36–43] Spherical shaped nanocellulose has also been developed and demonstrated for use in stabilizing the suspension of carbon nanotubes.[44–48] The biopolymer based nanocellulose-enabled membrane technology may not only be suitable for tackling global energy challenges, but it can also provide a new low-cost platform for the development of new energy storage and generation technologies.[49]

CNFs with a high aspect ratio possess excellent mechanical properties such as a Young's modulus of 138 GPa and an estimated strength of 2–3 GPa.[50,51] Additionally, the introduction of carboxyl and sulfonic acid groups enables proton conduction through nanocellulose membranes.[52–56] The fibrous morphology of CNFs can be used to fabricate membranes with controlled pore sizes that enable superior gas barrier properties comparable to Nafion.[57,58] Besides that, temperature is also an important factor affecting the fuel cell performance. High temperature operation leads to faster reaction kinetics, lower electrocatalyst loading, and improved water management, and can thereby further reduce the cost. However, higher temperature operation can impose a greater load on the membrane.[9,50,59]

There are several previous studies of cellulose/ionomer composite membranes.[60–63] Gadim *et al.* blended poly(4-styrene sulfonic acid) with bacterial cellulose and achieved an AC conductivity of 14 mS cm^{-1} at 98% relative humidity (RH) and a maximum power density of 40 mW cm^{-2} at 125 mA cm^{-2}.[64] Jiang *et al.* made Nafion/bacterial nanocellulose composite membranes which had a proton conductivity of 71 mS cm^{-1} and a power density of 106 mW cm^{-2} at 100% RH and at 30 °C.[56] Notably, there are only a few studies on functionalized nanocellulose membranes (*e.g.* TEMPO oxidized, sulfonated CNC) as the ionomer. Gadim *et al.* continued the study on Nafion/nanocellulose blends and determined an in-plane proton conductivity of 0.14 S cm^{-1} and a maximum power density of 40 mW cm^{-2} at 125 mA cm^{-2} at 98% RH and room temperature.[64] Hasani-Sadrabadi *et al.* prepared membranes with 5 wt% CNCs and Nafion and observed a maximum power density of 91 mW cm^{-2} at 70 °C in a direct methanol fuel cell, which was higher than pure Nafion as there was reduced methanol crossover.[65] Finally, Tritt-Goc *et al.* created a high temperature imidazole-doped CNC membrane that reached 2.7×10^{-2} S m^{-1} at 140 °C under dry conditions.[66] Bayer *et al.* first reported the use of pure CNF and CNC membranes and found superior gas barrier properties, but a significantly lower conductivity of 0.01 mS cm^{-1} for CNFs and ~15 mS cm^{-1} for Nafion at 100% RH and at 30 °C and power density of 0.79 mW cm^{-2} at 1.8 cm^{-2} for CNFs and ~450 mW cm^{-2} for Nafion.[13] The CNC membranes showed better performance but they were brittle due to high crystallinity and can be cracked from heat pressing.[59] Hence, CNFs with a high aspect ratio are required to maintain the mechanical strength of the membrane during the fuel cell operation.

In this work we have used a simple one step nitro-oxidation method which allows both resource and energy efficient production of carboxycellulose nanofibrils[27,67] from jute-fibers with two different forms of carboxylate (COONa) and carboxylic (COOH) groups. Here the carboxycellulose nanofibrils produced from the nitro-oxidation method are abbreviated as NOCNFs. This is the first report where the presence of ionic (COO^-, carboxylate) and non-ionic (COOH, carboxylic) groups in the nanopaper has been studied for their performance in PEMFCs. It is hypothesized that the nanopaper having a carboxylic group (COOH) will exhibit better performance in PEMFCs because of the following facts: (i) carboxylic acid can accept and donate the proton, and hence it will act as a better charge carrier, (ii) it can exhibit more intense hydrogen bonding that can lead to more crosslinking resulting in denser and mechanically strong nanopaper which can be applicable for high temperature operation, and (iii) carboxylic acid is hydrophilic that can lead to more water intake, and hence can allow more proton transfer. Additionally, none of the reports has demonstrated the use of a cost-effective, less-chemically oriented pathway to design the ionomer membrane. We are the first to explore NOCNFs in the preparation of such type of membranes useful in high tech applications (*e.g.*, fuel cell).

Experimental section

Untreated jute fibers (DP of extracted cellulose = 516) were provided by Toptrans Bangladesh Ltd. in Bangladesh. All samples were cut into small pieces of 3–5 cm in length and subsequently washed, but without further treatment. Analytical grade nitric acid (ACS reagent, 65%) and sodium nitrite (ACS reagent ≥ 97%) were purchased from Sigma Aldrich; sodium bicarbonate, hydrochloric acid (37%) and HPLC grade DI water were purchased from Fisher Scientific. All chemicals were used without further purification. Durapore membrane filter paper having a diameter of 47 mm and an average pore size of 0.1 μm was purchased from VWR.

Preparation of NOCNFs

NOCNFs were prepared by a previously reported nitro-oxidation method.[25] In brief, 10 g dried jute fibers were placed in a 2 L three-neck round-bottom flask, where 140 mL of nitric acid (60%) was added. When the samples became completely mixed in the acid, 4.6 g of sodium nitrite was added to the reaction mixture under continuous stirring. The addition of sodium nitrite causes the generation of red gases inside the flask, which were prevented from escaping by closing the mouths of round-bottom flasks with stoppers. The reaction was performed at 50 °C for 12 h and was then stopped by adding 500 mL of distilled water to the beaker. On equilibration of the final reaction mixture, the supernatant liquid was discarded to remove the excess acid, leaving behind the fibers at the bottom. After performing the first decantation process, a mixture of ethanol and water (1 : 2 ratio) was added to the fibers, and then the suspension was stirred. The sample was kept untouched until the liquid (supernatant) and solid fibers became separate layers. The supernatant was also decanted off to extract the fibers. The above decantation step was repeated 4–5 times, until the pH value of the fiber suspension reached above 2.5. This suspension was then transferred into a dialysis bag for 4–5 days until the conductivity of water reached below 5 μS. Once the

Published on 27 June 2022. Downloaded by State University of New York at Stony Brook on 7/17/2023 12:32:59 PM.

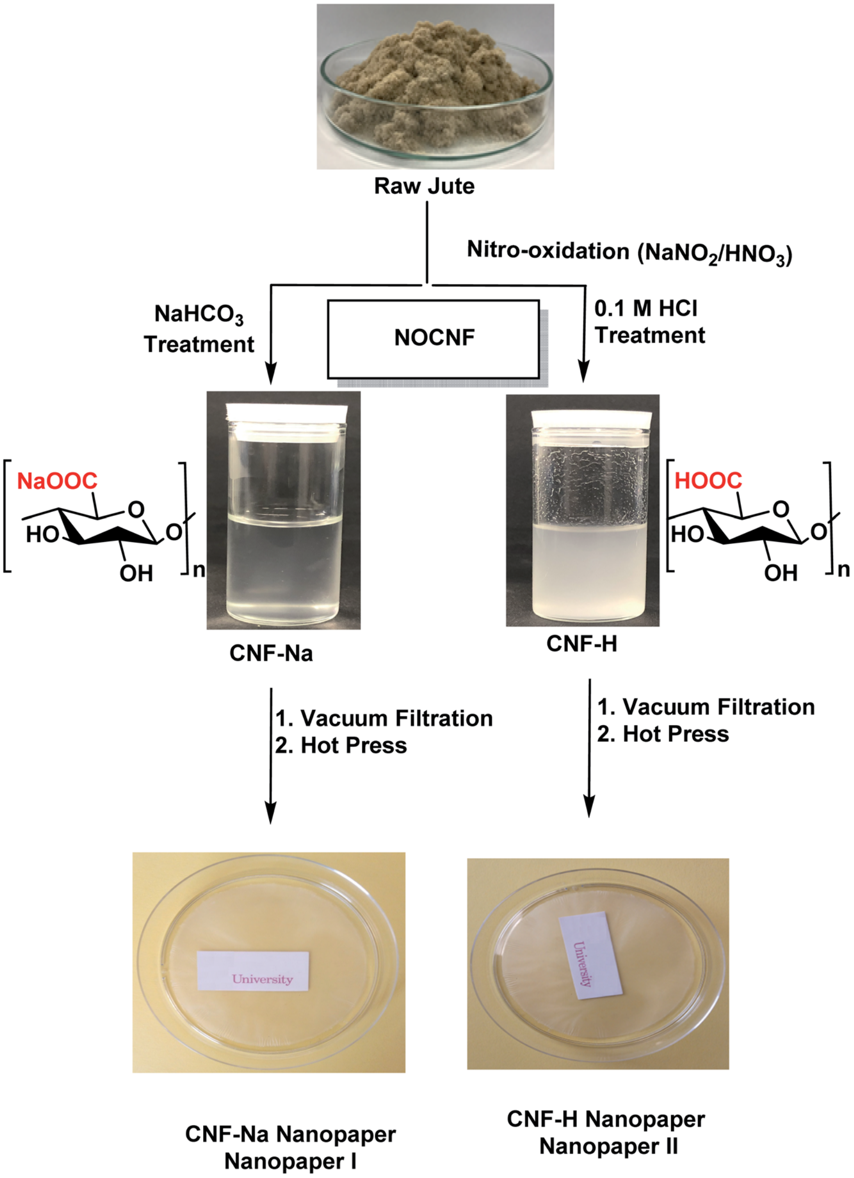

Fig. 1 Schematic preparation of nanopapers from raw jute fibers: nanopaper I and nanopaper II prepared by using CNF–Na and CNF–H respectively.

dialysis of the fiber suspension was finished the fibers were then treated with sodium bicarbonate (8 wt% sodium bicarbonates) to obtain a good dispersion, so that it can be easily homogenized to obtain the nanofiber suspension. Hence, the fibers were then passed using a high-pressure homogenizer (GEA Niro Soavi Panda Plus Bench top homogenizer) at 250 bar for 1 cycle. The obtained nanofibers were again dialyzed (using a dialysis bag, Spectra/Por, with MWCO: 6–8 kDa) and equilibrated for 2–4 days, until the conductivity of water reached below 5 μS. The obtained nanofibers possessed carboxylate groups (COO^-Na^+) and were termed CNF–Na.

One portion of the above nanofibers was then treated with 0.1 M hydrochloric acid until the pH of the suspension reached 2 and dialyzed for conversion of the –COONa functionality to –COOH. This nanofiber suspension was named CNF–H. The schematic diagram of the preparation of CNF–H and CNF–Na with two different functionalities using the nitro-oxidation approach is shown in Fig. 1.

Preparation of nanopapers

Nanocellulose suspensions in water (CNF–Na and CNF–H) with a 0.20 wt% concentration and volume of 200 mL were stirred separately for 3 h at 320 rpm to make the suspensions homogeneous. Then the suspensions of these CNFs were vacuum filtered by using a microfiltration assembly composed of a glass support. An Ultra-Ware glass funnel was connected to a vacuum pump, where the funnel was fitted with a Durapore membrane filter paper having a diameter of 47 mm and an average pore size of 0.1 μm. The aggregation of the nanofiber (CNF–H and CNF–Na) layer was formed continuously on top of the

Published on 27 June 2022. Downloaded by State University of New York at Stony Brook on 7/17/2023 12:32:59 PM.

membrane paper until a uniform wet sheet of nanopaper was achieved. The wet nanopaper sheet was then removed from the membrane paper, placed between two Kapton films and hot-pressed at 110 °C for 20 min. To avoid the wrinkling of the nanopaper edges, the resulting nanopaper was compressed under 2 kg of weight at room temperature for 10 h. The nanopaper prepared using the CNF–Na suspension was termed nanopaper I while nanopaper II developed using the CNF–H suspension was named nanopaper II. The thicknesses of nanopaper I and nanopaper II were in the range of 60–62 μm.

XPS analysis

The O 1s peak was calibrated to 532 eV and C 1s peak to 284.8 eV.

Proton conductivity

In-plane ion conductivity measurements were performed using a Scribner 740 MTS instrument for temperature and humidity control (under a N_2 atmosphere). Using a four-point probe, impedance was measured with an AC amplitude of 10 mV in a frequency range from 10 Hz to 10^5 Hz. Measurements were taken at 100% RH and at 30, 45, 60 and 80 °C. The samples were equilibrated to the appropriate testing conditions for 0.5 h prior to the impedance measurement. Resistance was determined from the high frequency *x*-intercept of the semicircle of Nyquist plots. Conductivity was calculated from the following equation:

$$\sigma = \frac{L}{A \times R} \tag{1}$$

where σ is the calculated conductivity, L is the length between the two inner probes, A is the cross-sectional area of the membrane and R is the resistance.

Fuel cell performance

The 5 cm^2 membrane electrode assembly (MEA) was made by hot-pressing two commercial carbon cloth electrodes (0.1 mg cm^{-2} Pt loading, fuel cell *etc.*) onto the opposite sides of nanopapers under the condition of 2 MPa at 140 °C for 1 min after waiting 5 min for the temperature to stabilize. The single cell performance was evaluated on a fuel cell test station (Fuel Cell Technology). The anode and cathode were fed with humidified H_2 and O_2 at 80 °C with 100% RH. H_2/O_2 gas fluxes were both controlled at 100 cm^3 min^{-1} and externally humidified at the dew point temperature. The performance test was conducted after 1 h of humidification. The backpressure for both the anode and cathode was varied from 0, 8 and 21 psi for the collection of polarization and power curves.

Results and discussion

Characterization of NOCNFs (CNF–H and CNF–Na)

The nitro-oxidation approach was designed to treat raw biomass, especially nonwood biomass, aiming to make the nanofiber extraction more facile, more sustainable, less chemically oriented, and less energy dependent. Based on our previous nitro-oxidation study the primary factor affecting the morphology and surface charge of NOCNFs was the amount and concentration of nitric acid used.[25,27] However, the decrease in nitric acid concentration to 60% could result in high aspect ratio NOCNFs having a significant portion of fiber length without changing the average width.[68] Typically, when a CNF has a good aspect ratio and high surface charge, the suspension can result in a homogeneous gel.[69] The CNF–Na sample obtained in the current study possess a surface charge of −117 mV in the form of COONa with a concentration of 0.94 mmol g^{-1}.

Furthermore, the –COONa groups of nanofibers were converted to –COOH groups to introduce highly acidic protons by treating the CNF–Na suspension with 0.1 M HCl until the pH of the suspension reached 2 followed by dialysis. The surface charge for these CNF–H nanofibers was found to be −72 mV. This indicates that this acidic treatment has led to a partial conversion of ionic $–COO^{-}Na^{+}$ groups to nonionic –COOH forms in CNF–H.

Fig. 2(i and ii) presents the TEM image of CNF–H and CNF–Na samples. The average length and width measured for CNF–Na were 511 ± 151 and 7.6 ± 1.9 nm while the average length and width obtained for CNF–H were 338 ± 127 and 7.7 ± 1.8 nm. The results indicate a decrease in the length of fibers on acidic treatment without a change in the fiber width. It is obvious that the acidic treatment of cellulosic fibers can cause the degradation of fibers by breakage of the 1,4-glycosidic bonds in cellulose chains.[45]

The AFM images of CNF–Na and CNF–H are presented in Fig. 2(iii and iv). It is observed that CNF–Na (Fig. 2(iii)) has not shown any aggregations of nanofibers, while CNF–H has presented strong accretion behavior likely due to the additional hydrogen bonding interaction between the cellulose chains resulting from COOH groups.[70] The photographs of CNF–Na and CNF–H suspensions shown in Fig. 1 further provide evidence of the accretion behavior of CNF–H. It is observed that the CNF–Na suspension is clearer and more transparent. However, the CNF–H suspension is nontransparent.

Surface functionality, chemical composition and thermal properties of nanopapers

The surface functionality of nanopaper I and II prepared from NOCNF suspensions was first carried out by FTIR. The FTIR spectra of both nanopapers are presented in Fig. 3(i). In these spectra, the dominant 3328 cm^{-1} peak due to the OH stretching and the weaker 2900 cm^{-1} peak due to the –CH symmetrical stretching (all from the cellulose component) were present in both nanopaper samples. The sharp peak that appears at around 1515 cm^{-1} in both nanopapers is due to C=C aromatic symmetrical stretching in the lignin unit, while peaks appear at 1739, 1460, 1240, and 810 cm^{-1} for the xylan and glucomannan of hemicellulose units.

The appearance of a sharp 1602 cm^{-1} peak in nanopaper I confirmed the presence of the C=O group of COONa functionality; while a sharp C=O absorption band at 1720 cm^{-1} is assigned to the C=O stretching of COOH functionality in nanopaper II.[70]

This journal is © The Royal Society of Chemistry 2022

Published on 27 June 2022. Downloaded by State University of New York at Stony Brook on 7/17/2023 12:32:59 PM.

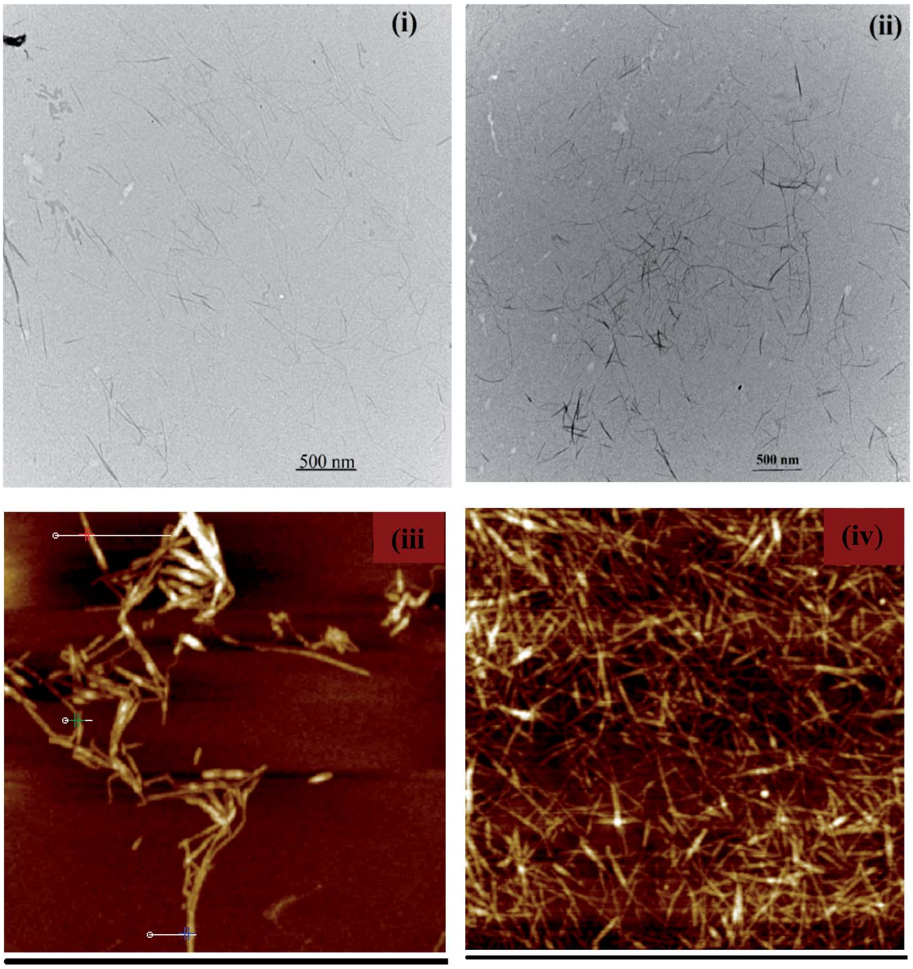

Fig. 2 TEM image of NOCNFs extracted from jute (i) CNF–Na (ii) CNF–H (taken at a scale bar of 500 nm and magnification of 3 290 000×); AFM images of NOCNFs (iii) CNF–H (iv) CNF–Na taken at 2.5 μm scale.

The thermogravimetric and derivative thermogravimetric analyses of nanopaper I and II are shown in Fig. 3(ii). The thermal degradation profiles of both the nanopapers exhibited almost similar and two major degradation steps, whereby the initial onset temperature (T_{onset}) was at 200 °C with 8.2 wt% weight loss, and the final offset temperature (T_{offset}) was at 305 °C with 48 wt% weight loss. The shifting of the T_{onset} value to a lower temperature of nanopapers (nanopaper I and II) as

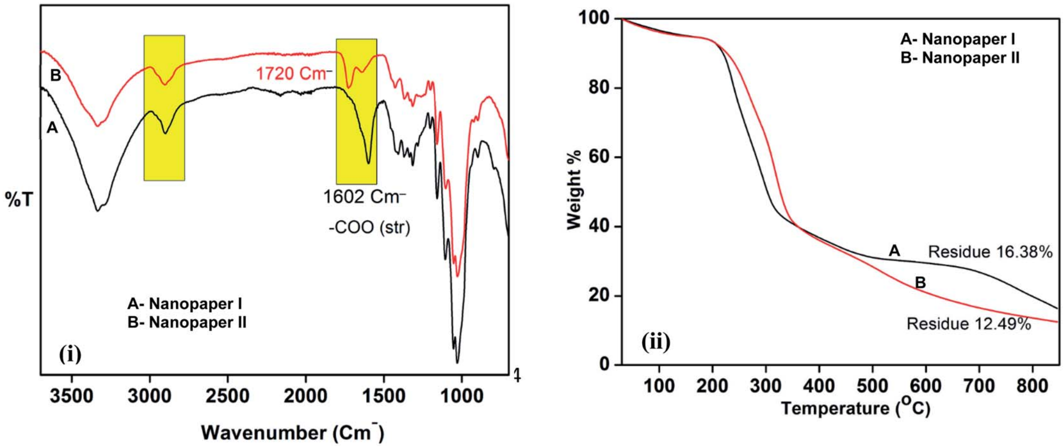

Fig. 3 (i) FTIR spectra of nanopaper I and II; (ii) TGA curves of nanopaper I and II.

Published on 27 June 2022. Downloaded by State University of New York at Stony Brook on 7/17/2023 12:32:59 PM.

compared to that of raw biomass indicates that the lower thermal stability of these nanopapers might be due to the presence of a thermally unstable anhydroglucoronic moiety in nanofibers, which could be degraded at a lower temperature (~200 °C) and release CO_2.[48] The major difference in the TGA profiles of nanopaper I and II is the amount of residual weight obtained at 550 °C. In the case of nanopaper I the residual weight was around 16.38%, while in the case of nanopaper II it was 12.49%. The higher residual weight% in the case of nanopaper I can be explained by the presence of residual metal oxide resulting from the thermal decomposition of COONa functionality.

Fig. 4(i) shows the XPS wide scan of nanopaper I and II. The Na KLL Auger peak was observed at 497 eV in nanopaper I. Using the sensitivity factor for C 1s and O 1s of 1.00 and 2.93 respectively, the elemental composition of nanopaper I was calculated to be 62.4% carbon and 34.3% oxygen. The elemental composition of nanopaper II was calculated to be 67.2% carbon and 32.4% oxygen. The C 1s peak of both the nanopapers can be deconvoluted into four smaller peaks. Fitting was performed using a Shirley background, Gaussian curve fitting, and constraining peak position, area, and full width at half maximum (FWHM). From greatest to lowest relative area shown in Fig. 4(ii), the C–C and C–H peaks corresponded to the cellulose backbone ring and hydrocarbon bonding. The C–OH peak is attributed to carbon bonded alcohol groups in the cellulose chain. The O–C–O peak appeared due to acetal groups while the O=C–O peak is from carboxyl groups. The O 1s peak of nanopaper I and II was deconvoluted into four peaks as shown in Fig. 4(iii). The O=C–O peak corresponded to carbonyl oxygen of the acid, C–OH is attributed to the alcohol group, C–O–C–O resulted from the acetal group and O–C=O was assigned to singly bonded oxygen of the acid. On comparing the XPS spectra of both nanopapers shown in Fig. 4(iii), the O–C=O and O=C–O contributions were estimated approximately equally to be in agreement with the theoretical structure of carboxylated cellulose. Moreover, the largest contribution was from the C–OH bond (~40%) which confirms that not all alcohols of cellulose were oxidized, likely secondary alcohol groups remained. Fitting for the carboxylic acid of both C 1s and O 1s was based on the carboxylate content calculated from conductometric titration; 0.94 mmol of carboxylate per gram of cellulose. Because cellulose has a structure of $C_6H_{10}O_5$, it is estimated that six out of every twenty-one atoms are carbon. And for every mole of carboxylate, there is one mole of carbon. On these assumptions, we estimated the C 1s O=C–O contribution to be 3.9%. A similar estimate was made for each oxygen of the O 1s O=C–O, while also constraining the peak areas to be equal during fitting.[71]

The contact angle measurement for nanopaper I and II is presented in Fig. S1 (ESI†). The average contact angle observed for nanopaper I and nanopaper II was 47.2° and 34.4° respectively. The lower contact angle value for nanopaper II indicates more hydrophilicity as compared to nanopaper I showing the high water intake capability of nanopaper II. This further confirms the presence of highly acidic and hydrophilic COOH groups on the surface of nanopaper II.[72]

WAXD measurements were carried out as shown in Fig. 5(i) to confirm the crystallinity index and the crystal structure of nanopapers. The WAXD patterns of nanopapers indicate that both the nanopapers have exhibited a cellulose I structure with diffraction peaks at 2θ angles of 16.5°, 22.7°, and 35.1° corresponding to (110), (200), and (004) reflections, respectively. This further provides evidence that the change of COONa to COOH functionality in NOCNFs did not change the crystal structure of the cellulose chain. The crystallinity index (CI) calculated from the WAXD data for nanopaper I was 77%, while that for nanopaper II was 60.9%. The lower crystallinity of nanopaper II could be because of the additional acid treatment that was employed to convert the COONa groups in NOCNFs to COOH.

Solid state ^{13}C CPMAS NMR spectra of nanopaper I and nanopaper II are shown in Fig. 5(ii). The NMR spectra of both the nanopapers show the distinct peaks of the cellulose I chain as follows: (i) peaks between 60 and 70 ppm belong to C6 carbon of the primary alcohol group, (ii) a group of peaks in between 70 and 80 ppm were attributed to the C2, C3, and C5 carbons, (iii) peak between 80 and 95 ppm was associated with C4 carbon, (iv) peaks between 100 and 110 ppm were due to the anomeric carbon C1.[58] Most importantly, the peak corresponding to carboxylate carbon for nanopaper I appeared at 178 ppm while for nanopaper II, it shifted more downfield at 172 ppm. This is

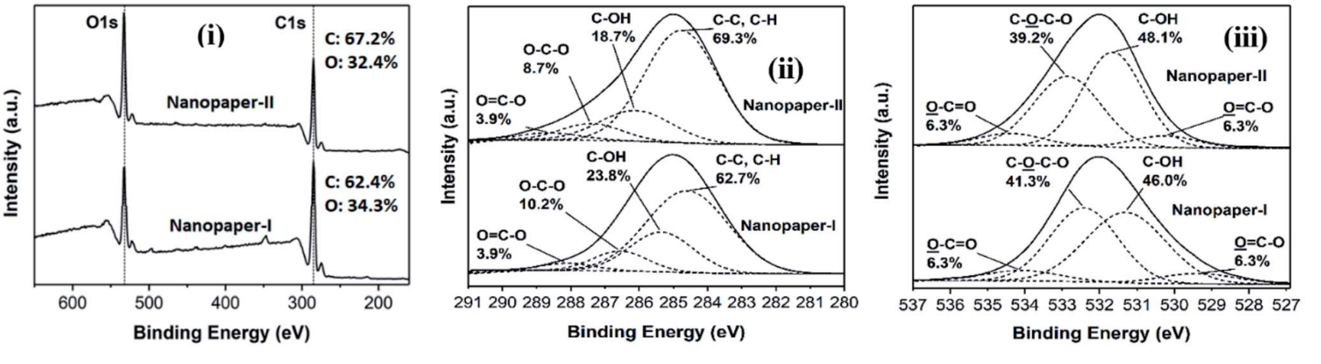

Fig. 4 (i) XPS wide scan spectra of nanopaper I and II and elemental composition. (ii) Deconvoluted C 1s spectra of nanopaper I and II with relative bond distribution. (iii) Deconvoluted O 1s spectra of nanopaper I and II with relative bond distribution.

This journal is © The Royal Society of Chemistry 2022

Published on 27 June 2022. Downloaded by State University of New York at Stony Brook on 7/17/2023 12:32:59 PM.

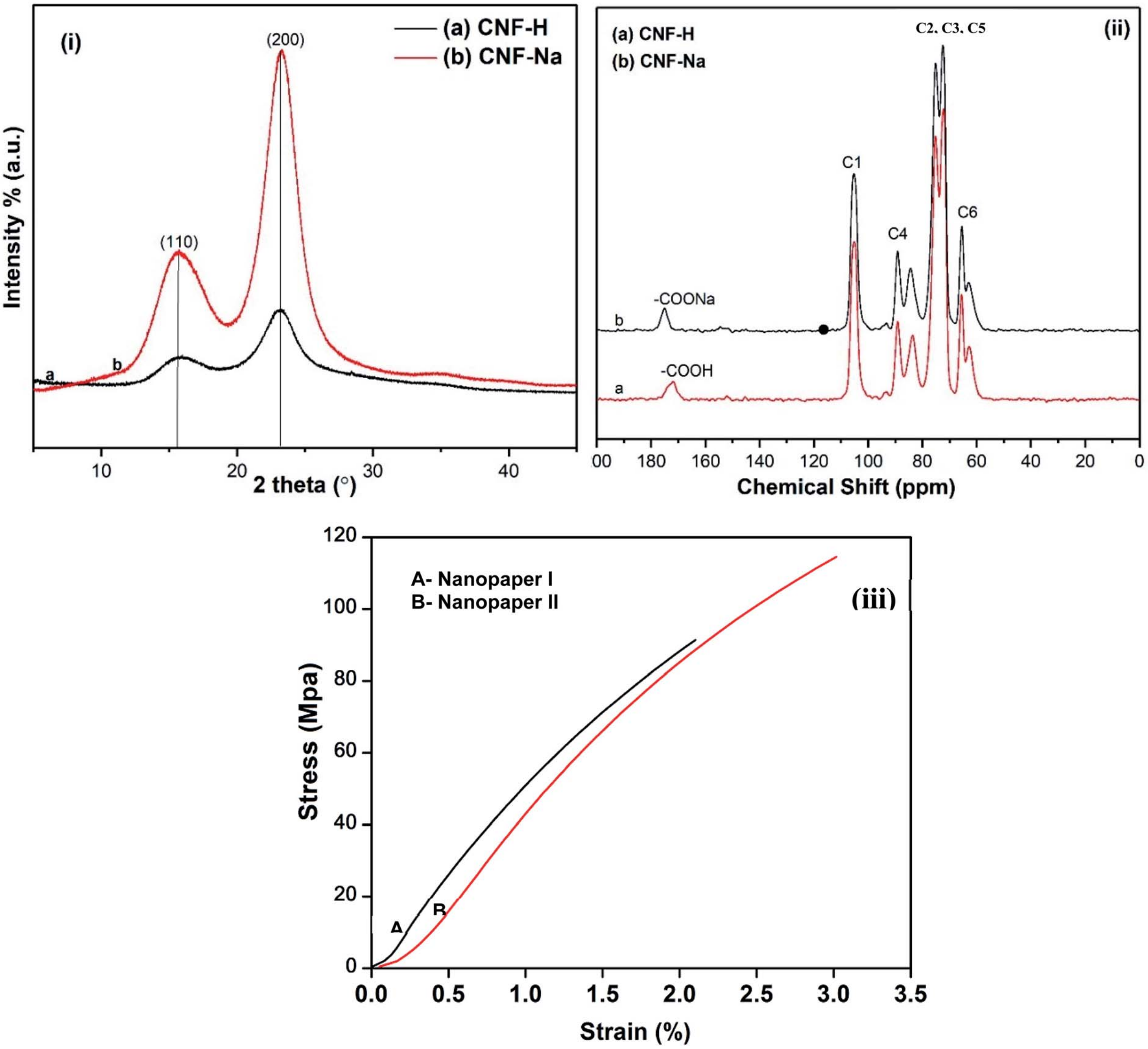

Fig. 5 (i) WAXD patterns of nanopaper I and II. (ii) ^{13}C CPMAS NMR spectra of nanopaper I and II. (iii) Tensile curves of nanopaper I and II.

because nanopaper I consists of COONa groups where Na$^+$ ions are more electropositive than H$^+$ of COOH in nanopaper II.

Tensile properties of two nanopapers I and II are shown in Fig. 5(iii). nanopaper I was prepared using CNF–Na whose average *L* and *W* was 511 ± 151 and 7.6 ± 1.9 nm, respectively while nanopaper II prepared by using CNF–H showed an average *L* and *W* in the range of 338 ± 127 and 7.7 ± 1.8 nm respectively. Hence, nanopaper I exhibited a higher aspect ratio (*L*/*D*) of 67.2 as compared to the aspect ratio of nanopaper II which was 43.8. The higher aspect ratio for nanopaper II should lead to excellent mechanical properties.[69] However, in this study we have observed the opposite trend where nanopaper I comprised of high aspect ratio CNF–Na showed a lower tensile strength of 89 ± 1.2 MPa with an elongation at break of 2.2 ± 0.2%, while nanopaper II consisting of low aspect ratio CNF–H exhibited a high tensile strength of 112 ± 2 MPa with elongation at break ratio of 3.0 ± 0.2%. The most probable reason for this opposite trend could be the presence of COOH groups in nanopaper II that has induced strong hydrogen bonding owing to its strong tensile strength.

Surface morphology, BET surface area, and mechanical properties of nanopapers

Photographs of the two nanocellulose suspensions (CNF–Na and CNF–H) and their corresponding nanopaper I and II are shown in Fig. 1. The suspension of CNF–Na looks clear and highly suspended due to the presence of ionic –COONa groups, while the CNF–H suspension appears more blurred likely due to the aggregation of nanofibers *via* hydrogen bonding induced by their –COOH groups. Similarly, nanopaper I looks more transparent than nanopaper II.

SEM images in Fig. 6 present the exterior and interior morphology of nanopaper I and II. Both the nanopapers consist of a network of randomly interwoven fibers. The surface of nanopaper I looks smooth with evenly distributed fibers while the surface of nanopaper II appeared rough likely due to highly

Published on 27 June 2022. Downloaded by State University of New York at Stony Brook on 7/17/2023 12:32:59 PM.

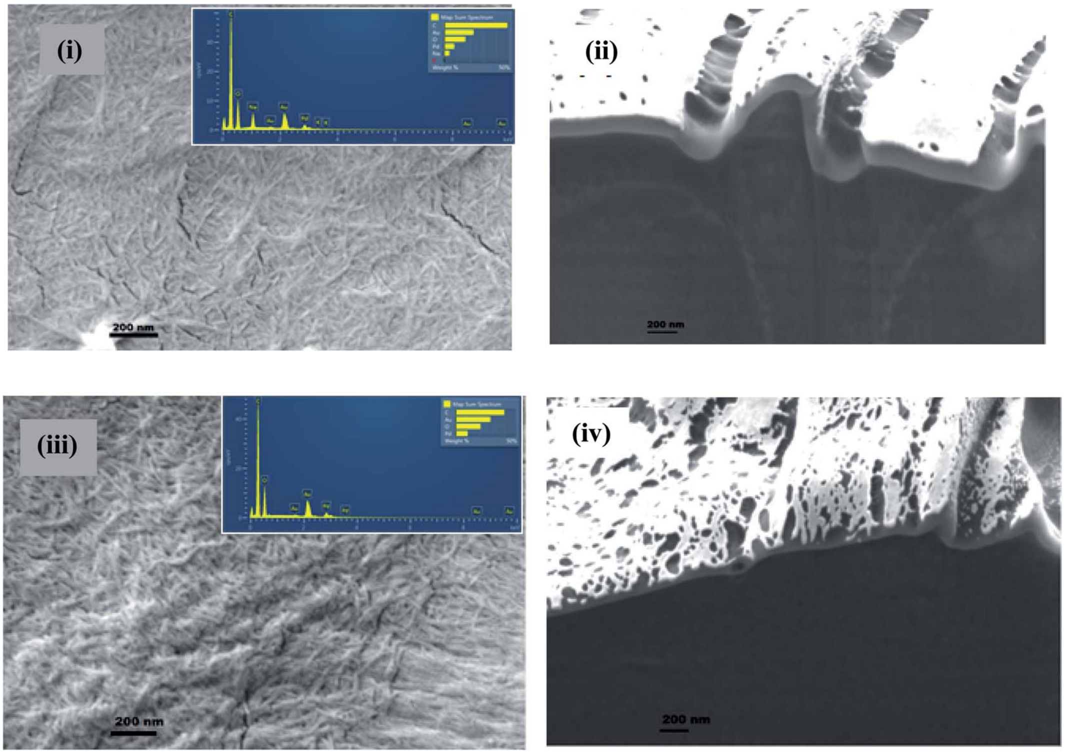

Fig. 6 (i) SEM image and EDX elemental mapping of nanopaper I (ii) SEM image of cross section of nanopaper I (iii) SEM image and EDX elemental mapping of nanopaper II (iv) SEM image of cross-section of nanopaper II.

crosslinked hydrogen bonded fibers by COOH functional groups as discussed in the FTIR section. The difference between the surface morphologies of both the nanopapers is quite depictive in their respective cross-section SEM images. The cross-section SEM image of nanopaper I shows big pores along with a few small tiny pores on the smooth surface, while on the surface of nanopaper II more evenly distributed pores were observed which are smaller in size compared to nanopaper I, which further evidence that nanopaper II is comprised of highly crosslinked and interconnected fibers resulting in its smooth and denser membrane.

The BET measurement for nanopaper I and nanopaper II is presented in Fig. S2 in the ESI.† The measured surface area for nanopaper I and II was 1.83 and 0.87 m^2 g^{-1} respectively. The lower surface area value for nanopaper II compared to nanopaper I indicates that the nanopaper II structure is comparatively denser due to the highly crosslinked nanofiber network which is clearly seen in the SEM image of nanopaper II. Both the nanopapers I and II possessed very small total mesopore volumes of 0.006 and 0.002 cm^3 g^{-1}, respectively (presented in Fig. S3 in the ESI†). The low pore volume indicates the good gas barrier properties of both nanopapers I and II, and allows them to be suitable for hydrogen fuel cell applications.[59]

Fuel cell performance

Until now a functionalized nanocellulose membrane with COOH functionality in PEMFCs has not been reported in the literature to the best of our knowledge. Both the nanopapers have shown excellent performance as proton conducting electrolytes and contributed to the performance of the assembled fuel cell. Additionally, the effect of back pressure was studied. The high backpressure has enhanced the power output of the MEA in both cases. For example, nanopaper I and II exhibited an open circuit voltage (OCV) of 0.70 and 0.85 V respectively, while the OCV for commercial membrane based fuel cells such as Nafion was found to be 0.94 V when measured under similar conditions.[6] This confirms that the NOCNF nanopaper based paper electrolyte works competently in transporting protons and blocking electrons while maintaining a very low hydrogen crossover. A probable reason for nanopapers to demonstrate such properties is their dense and cross-linked surface topography caused by their surface functionalities (COOH and COONa).

Fig. 7(i and ii) shows the polarization curves of nanopaper I and II. The OCV found for nanopaper I was 0.70 V which immediately dropped to 0.60 V on increasing the current. This type of behavior exhibits its activation losses during the operation. A similar trend has been reported for the commercial Nafion membrane.[15] In the case of nanopaper I, a maximum power density of 1.8 mW cm^{-2} at a current density of 4.1 mA cm^{-2} was achieved when 8 psi of back pressure was applied. A significant increment in current density to 8.9 mA cm^{-2} was observed when back pressure increased to 21 psi. Notably, no OCV and power generation was observed in nanopaper I at 0 back pressure which is likely due to its low proton conductance and higher resistance which is discussed later in the proton conduction section.

This journal is © The Royal Society of Chemistry 2022

Published on 27 June 2022. Downloaded by State University of New York at Stony Brook on 7/17/2023 12:32:59 PM.

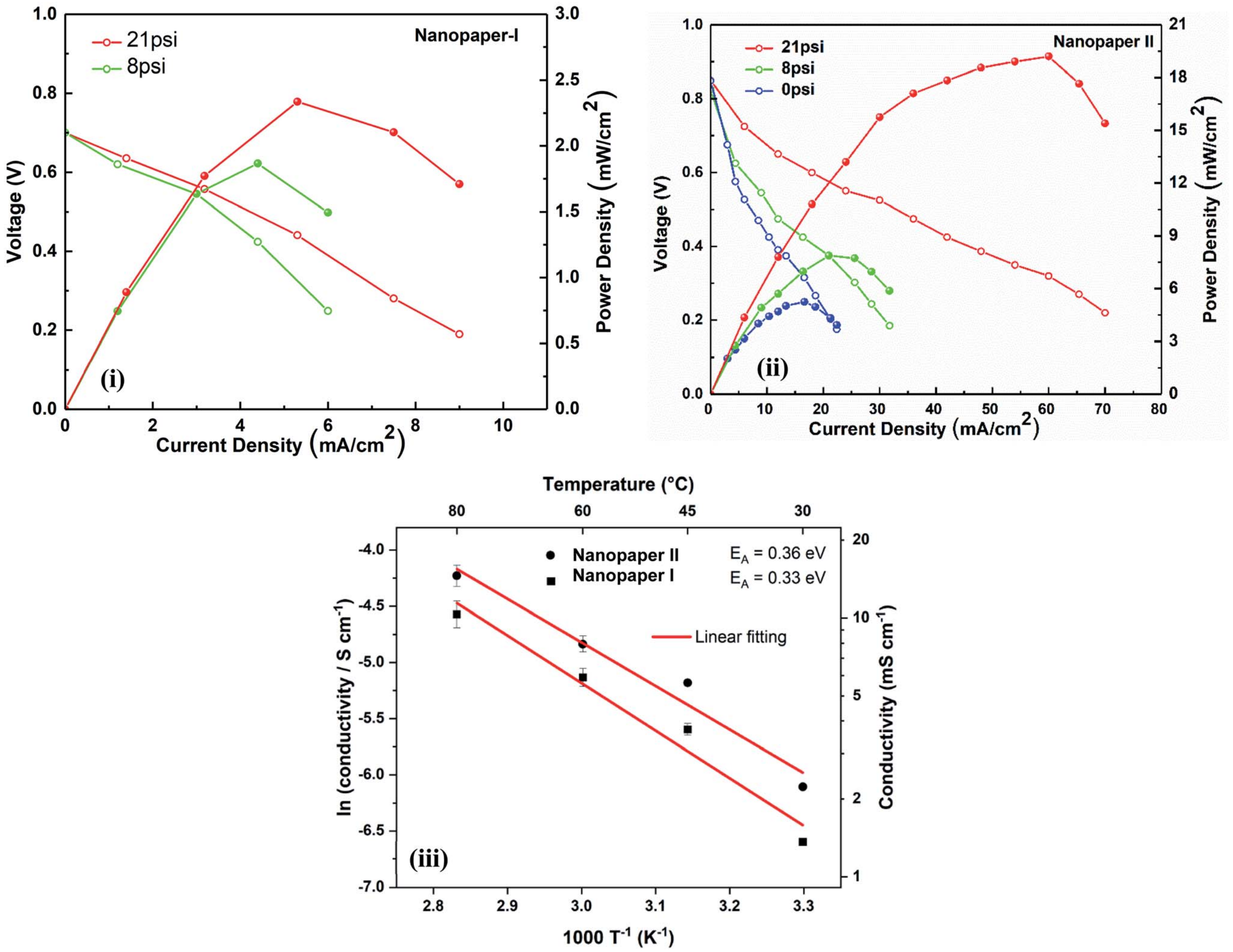

Fig. 7 Polarization and power curves of (i) nanopaper I and (ii) nanopaper II under various oxygen pressure conditions; (iii) Arrhenius plot of the conductivity of nanopaper I and II (at 100% RH) with activation energies.

For nanopaper II, three polarization curves were obtained at three different back pressures of 0, 8, and 21 psi at an operating temperature of 80 °C which are shown in Fig. 7(ii). In the case of nanopaper-II, the OCV measured was 0.87 V which is higher compared to nanopaper I. The increased OCV was due to more strength and high proton conduction due to the presence of highly acidic COOH groups on the surface of the nanofibers in nanopaper II, while nanopaper I comprised of COONa groups. The OCV for nanopaper II remained constant at 0.87 V at all three back pressures of 0, 8 and 21 psi used during the experiments. It showed maximum power densities of 4.1, 6.2 and 19.2 mW cm^{-2} when 0, 8 and 21 psi back pressure were applied, respectively. The highest power density of 19.1 mW cm^{-2} at a current density of 57.2 mA cm^{-2} was achieved for nanopaper II, when 21 psi of back pressure was applied. This is about 5 times higher than the power density achieved at 0 psi back pressure and 3 times higher than the power density attained at 8 psi. Additionally, the maximum current density observed for nanopaper II is about 10 times higher than the maximum current density observed for nanopaper I. The overall results indicate that nanopaper II shows better conductance in comparison to nanopaper I. This could be because of the following reasons: (i) the presence of highly acidic –COOH groups on the surface of nanopaper II has aided in better proton transfer and (ii) the uniform and highly dense surface in nanopaper II caused by a high degree of crosslinking from –COOH groups may have accounted for preventing hydrogen gas oozing through the membrane while allowing proton migration, which resulted in a higher performance (*e.g.*, high OCV).[59] These results fully support our hypothesis of using COOH functionalized nanopaper in PEMFCs.

The high backpressure has led to high power output of the MEA in both cases which is likely due to a decrease in cell ability to drain out water because of enhanced RH in the cathode channel on applying high back pressure leading to high membrane water content which aids in improvement in the PEMFC performance.[73] However, the OCV of the nanopaper II cell remained at around 0.87 V regardless of the variation in back pressure (Fig. 7(ii)) which is 100 mV higher than the nanopaper I based fuel cell. Notably, the fuel cell performance

Published on 27 June 2022. Downloaded by State University of New York at Stony Brook on 7/17/2023 12:32:59 PM.

of nanopaper II is significantly higher than that of the similar TEMPO oxidized nanofiber membrane system reported previously in the literature.[13] The TEMPO oxidized nanofiber based membrane possessed COONa functionality[13] like nanopaper I. In summary, in this study we have proven that the functionality changes of COONa in nanopaper I to COOH in nanopaper II have tremendously improved the performance of the MEA.

A durability measurement was performed on the nanopaper II based fuel cell at 80 °C at a constant current of 11 mA and an initial voltage of 0.6 V for 24 h and is presented in Fig. S4 in the ESI.† Only a slight cell voltage fluctuation by ±0.5 V was observed. This fluctuation could be the result of small pressure variations that generally occurred during the operation. Overall, this measurement confirms the steady operation of the nanopaper II fuel cell at 80 °C and provides a new insight into substituting the synthetic membrane with a sustainable and cost-effective high-temperature nanopaper membrane in the operation of PEMFCs.

The slope of the Arrhenius plot can be used to determine the activation energy (E_A) which can provide vital information about the possible mechanism for proton transportation. High proton conductivity of membranes plays an important role in decreasing ohmic resistance and in increasing cell performance in a fuel cell.[74] Nanopaper I and II were tested at 100% RH to investigate their proton conduction mechanisms. Fig. 7(iii) displays the Arrhenius plot of the conductivity for both nanopapers measured at variable operating temperatures of 30, 45, 60 and 80 °C. It was observed that with an increase in temperature from 30 to 80 °C, the conductivity of nanopaper I and II increased from 1.4 to 10.4 mS cm^{-1} and from 2.2 to 14.6 mS cm^{-1}, respectively. The slope from a linear fit of the data points allows the E_A of proton conduction to be calculated. In the literature, two mechanisms, vehicular and Grotthuss have been described to explain the proton transport under humidified conditions through the membrane.[59] The vehicular mechanism involves the transport of a charge by a hydronium ion that generally leads to a higher E_A while the Grotthuss mechanism describes the transport of protons through the bonding and de-bonding in a hydrogen bonded network, and hence leads to a low E_A. In the present study, nanopaper I and II have shown an E_A of 0.36 and 0.33 eV, respectively while the nanopapers from CNCs and TEMPO oxidized nanofibers reported earlier have shown an E_A of 0.21 and 0.24 eV[13] and Nafion shows an E_A of 0.16 eV. Nafion follows Grotthuss like proton transport where it supports proton transport through a complete hydrogen bonding network.[13] The E_A measurements indicate that nanopaper II has better hydrogen bonded ion conduction networks causing more facile proton conduction because of the presence of COOH functionality. The above results indicate that NOCNF based nanopapers are very importnat for the development of sustainable PEM fuel cells. As described, the nanopapers used in this study are derived from NOCNFs which are extracted using the nitro-oxidation method. Nitro-oxidation is highly efficient in generating negative surface charge on fibers which is owed to nanofibers with an ample amount of polyelectrolyte polymeric chains having COOH groups. In this way NOCNFs offer alternatives to synthetic PEM fuel cell membranes (*e.g.*, Nafion) for membrane design.

Conclusions

Plant-based nanocelluloses were extracted from jute fibers using a simple, cost-effective and less chemically oriented 'nitro-oxidation' approach and further two nanopapers with different functionalities of COONa (nanopaper I) and COOH (nanopaper II) were fabricated. These nanopapers displayed proton conductivity that is highly dependent on surface functionality and temperature. Among the two nanopapers, nanopaper II has presented better proton conduction and fuel cell performance. This is attributed to highly acidic –COOH groups which have not only served as proton donors/charge carriers but also provided a dense and strong structure to nanopapers through crosslinking of nanofibers by numerous hydrogen bonding interactions. The maximum conductivity observed for nanopaper II was 14.6 mS cm^{-1} at 80 °C (at 100% RH). The higher conductivity of nanopaper II even at high temperature (80 °C) is ascribed to COOH groups introduced during the nitro-oxidation that acted as charge carriers. Fuel cells utilizing NOCNF nanopapers were fabricated and tested at 80 °C and 100% RH using hydrogen fuel. As expected, because of the higher conductivity, dense surface, hydrophilicity and tensile strength, fuel cells incorporating nanopaper II displayed good performance with a power density of 19.1 mW cm^{-2} compared to those incorporating nanopaper I which have exhibited a power density of 5.8 mA cm^{-2}. A durability test on nanopaper II confirms its stability in fuel cell operation at 80 °C for 24 h. These results show that nitro-oxidized nanocellulose paper can be applied as a sustainable, environment-friendly, and inexpensive source to fabricate high-temperature ionomer membranes useful in electrochemical devices (*e.g.*, fuel cells).

Conflicts of interest

There are no conflicts to declare.

Acknowledgements

The authors acknowledge financial support from the Polymer Program of the Division of Materials Research in the National Science Foundation (DMR-1808690). The authors would like to thank Dr Jim Quinn (Materials Science and Engineering-Stony Brook University) for SEM analysis, Tomas Rosen (Stony Brook University) for helping with the TOC image and Dr Chung-Chueh Chang (ThINc-Stony Brook University) for TGA, TEM and AFM analysis.

References

1 WHO, 2015, **https://www.un.org/en/development/desa/news/population/2015-report.html**, retrived 24 June, 2020.
2 M. Winter and R. J. Brodd, *Chem. Rev.*, 2004, **104**, 4245–4270.
3 C.-Y. Wang, *Chem. Rev.*, 2004, **104**, 4727–4766.

This journal is © The Royal Society of Chemistry 2022

Published on 27 June 2022. Downloaded by State University of New York at Stony Brook on 7/17/2023 12:32:59 PM.

4 P. P. Edwards, V. L. Kuznetsov, W. I. F. David and N. P. Brandon, *Energy Policy*, 2008, **36**, 4356–4362.

5 I. Staffell, D. Scamman, A. Velazquez Abad, P. Balcombe, P. E. Dodds, P. Ekins, N. Shah and K. R. Ward, *Energy Environ. Sci.*, 2019, **12**, 463–491.

6 L. Wang, S. Bliznakov, R. Isseroff, Y. Zhou, X. Zuo, A. Raut, W. Wang, M. Cuiffo, T. Kim and M. H. Rafailovich, *Appl. Energy*, 2020, **261**, 114277.

7 X. Xiao, H.-q. Xia, R. Wu, L. Bai, L. Yan, E. Magner, S. Cosnier, E. Lojou, Z. Zhu and A. Liu, *Chem. Rev.*, 2019, **119** 9509–9558.

8 K. V. Kordesch and G. R. Simader, *Chem. Rev.*, 1995, **95**, 191–207.

9 L. Wang, X. Zuo, A. Raut, R. Isseroff, Y. Xue, Y. Zhou, B. Sandhu, T. Schein, T. Zeliznyak, P. Sharma, S. Sharma, B. S. Hsiao and M. H. Rafailovich, *Sustainable Energy Fuels*, 2019, **3**, 2725–2732.

10 K. A. Mauritz and R. B. Moore, *Chem. Rev.*, 2004, **104**, 4535–4586.

11 P. Sapkota, C. Boyer, R. Dutta, C. Cazorla and K.-F. Aguey-Zinsou, *Sustainable Energy Fuels*, 2020, **4**, 439–468.

12 T. Wilberforce, A. Alaswad, A. Palumbo, M. Dassisti and A. G. Olabi, *Int. J. Hydrogen Energy*, 2016, **41**, 16509–16522.

13 T. Bayer, B. V. Cunning, R. Selyanchyn, M. Nishihara, S. Fujikawa, K. Sasaki and S. M. Lyth, *Chem. Mater.*, 2016, **28**, 4805–4814.

14 R. S. L. Yee, R. A. Rozendal, K. Zhang and B. P. Ladewig, *Chem. Eng. Res. Des.*, 2012, **90**, 950–959.

15 A. K. Sahu, S. Pitchumani, P. Sridhar and A. K. Shukla, *Bull. Mater. Sci.*, 2009, **32**, 285–294.

16 S. Salimi, R. Sotudeh-Gharebagh, R. Zarghami, S. Y. Chan and K. H. Yuen, *ACS Sustainable Chem. Eng.*, 2019, **7**, 15800–15827.

17 H. M. C. Azeredo, M. F. Rosa and L. H. C. Mattoso, *Ind. Crops Prod.*, 2017, **97**, 664–671.

18 B. Thomas, M. C. Raj, A. B. B, R. M. H, J. Joy, A. Moores, G. L. Drisko and C. Sanchez, *Chem. Rev.*, 2018, **118**(24), 11575–11625.

19 P. R. Sharma, S. K. Sharma, T. Lindström and B. S. Hsiao, *Adv. Sustainable Syst.*, 2020, **4**, 1900114.

20 P. R. Sharma, S. K. Sharma, T. Lindström and B. S. Hsiao, *Adv. Sustainable Syst.*, 2020, **4**, 1900114.

21 D. Klemm, E. D. Cranston, D. Fischer, M. Gama, S. A. Kedzior, D. Kralisch, F. Kramer, T. Kondo, T. Lindström, S. Nietzsche, K. Petzold-Welcke and F. Rauchfuß, *Mater. Today*, 2018, **21**, 720–748.

22 P. R. Sharma, S. K. Sharma, R. Antoine and B. S. Hsiao, *ACS Sustainable Chem. Eng.*, 2019, **7**, 6140–6151.

23 H. Chen, S. K. Sharma, P. R. Sharma, H. Yeh, K. Johnson and B. S. Hsiao, *ACS Omega*, 2019, **4**, 22008–22020.

24 C. Zhan, Y. Li, P. R. Sharma, H. He, S. K. Sharma, R. Wang and B. S. Hsiao, *RSC Adv.*, 2019, **9**, 40565–40576.

25 P. R. Sharma, B. Zheng, S. K. Sharma, C. Zhan, R. Wang, S. R. Bhatia and B. S. Hsiao, *ACS Appl. Nano Mater.*, 2018, **1**, 3969–3980.

26 P. R. Sharma, A. Chattopadhyay, C. Zhan, S. K. Sharma, L. Geng and B. S. Hsiao, *Cellulose*, 2018, **25**, 1961–1973.

27 P. R. Sharma, R. Joshi, S. K. Sharma and B. S. Hsiao, *Biomacromolecules*, 2017, **18**, 2333–2342.

28 X. Xu, F. Liu, L. Jiang, J. Y. Zhu, D. Haagenson and D. P. Wiesenborn, *ACS Appl. Mater. Interfaces*, 2013, **5**, 2999–3009.

29 T. Saito, S. Kimura, Y. Nishiyama and A. Isogai, *Biomacromolecules*, 2007, **8**, 2485–2491.

30 D. da Silva Perez, S. Montanari and M. R. Vignon, *Biomacromolecules*, 2003, **4**, 1417–1425.

31 A. Isogai, T. Saito and H. Fukuzumi, *Nanoscale*, 2011, **3**, 71–85.

32 C. B. Hollabaugh, L. H. Burt and A. P. Walsh, *Ind. Eng. Chem.*, 1945, **37**, 943–947.

33 N. V. Lukasheva, D. A. Tolmachev and M. Karttunen, *Phys. Chem. Chem. Phys.*, 2019, **21**, 1067–1077.

34 S. Yang, Q. Xie, X. Liu, M. Wu, S. Wang and X. Song, *RSC Adv.*, 2018, **8**, 3619–3625.

35 Z. Zhang, G. Sèbe, D. Rentsch, T. Zimmermann and P. Tingaut, *Chem. Mater.*, 2014, **26**, 2659–2668.

36 M. Kaushik and A. Moores, *Green Chem.*, 2016, **18**, 622–637.

37 K. Kanomata, N. Fukuda, T. Miyata, P. Y. Lam, T. Takano, Y. Tobimatsu and T. Kitaoka, *ACS Sustainable Chem. Eng.*, 2020, **8**, 1185–1194.

38 S. Hu, F. Jiang and Y.-L. Hsieh, *ACS Sustainable Chem. Eng.*, 2015, **3**, 2566–2574.

39 H. Golmohammadi, E. Morales-Narváez, T. Naghdi and A. Merkoçi, *Chem. Mater.*, 2017, **29**, 5426–5446.

40 D. Trache, A. F. Tarchoun, M. Derradji, T. S. Hamidon, N. Masruchin, N. Brosse and M. H. Hussin, *Front. Chem.*, 2020, **8**, 392.

41 N. Mahfoudhi and S. Boufi, *Cellulose*, 2017, **24**, 1171–1197.

42 J. Herrera-Morales, K. Morales, D. Ramos, E. O. Ortiz-Quiles, J. M. López-Encarnación and E. Nicolau, *ACS Omega*, 2017, **2**, 7714–7722.

43 Z. Karim, M. Hakalahti, T. Tammelin and A. P. Mathew, *RSC Adv.*, 2017, **7**, 5232–5241.

44 P. R. Sharma and A. J. Varma, *Carbohydr. Polym.*, 2014, **114**, 339–343.

45 P. R. Sharma and A. J. Varma, *Chem. Commun.*, 2013, **49**, 8818–8820.

46 P. R. Sharma, S. Kamble, D. Sarkar, A. Anand and A. J. Varma, *Int. J. Biol. Macromol.*, 2016, **87**, 460–465.

47 P. R. Sharma, P. R. Rajamohanan and A. J. Varma, *Carbohydr. Polym.*, 2014, **113**, 615–623.

48 P. R. Sharma and A. J. Varma, *Carbohydr. Polym.*, 2014, **104**, 135–142.

49 R. Das, T. Lindström, P. R. Sharma, K. Chi and B. S. Hsiao, *Chem. Rev.*, 2022, **122**, 8936–9031.

50 W. Chen, H. Yu, S.-Y. Lee, T. Wei, J. Li and Z. Fan, *Chem. Soc. Rev.*, 2018, **47**, 2837–2872.

51 R. Mangayil, S. Rajala, A. Pammo, E. Sarlin, J. Luo, V. Santala, M. Karp and S. Tuukkanen, *ACS Appl. Mater. Interfaces*, 2017, **9**, 19048–19056.

52 X. Xu, R. Li, C. Tang, H. Wang, X. Zhuang, Y. Liu, W. Kang and L. Shi, *Carbohydr. Polym.*, 2018, **184**, 299–306.

53 Z. Cai, R. Li, X. Xu, G. Sun, X. Zhuang, Y. Liu and B. Cheng, *Polymer*, 2018, **156**, 179–185.

Published on 27 June 2022. Downloaded by State University of New York at Stony Brook on 7/17/2023 12:32:59 PM.

54 X. Hou, Z. Liu, Y. Wei, Q. Zhao, J. Dong, B. Liu, Z. Sun, T. Shi, M. Zhang and W. Hu, *Solid State Ionics*, 2017, **311**, 31–40.

55 C. Ni, H. Wang, Q. Zhao, B. Liu, Z. Sun, M. Zhang, W. Hu and L. Liang, *Solid State Ionics*, 2018, **323**, 5–15.

56 G. Jiang, J. Qiao and F. Hong, *Int. J. Hydrogen Energy*, 2012, **37**, 9182–9192.

57 S. Banerjee and D. E. Curtin, *J. Fluorine Chem.*, 2004, **125**, 1211–1216.

58 H. Fukuzumi, S. Fujisawa, T. Saito and A. Isogai, *Biomacromolecules*, 2013, **14**, 1705–1709.

59 C. Vilela, A. J. D. Silvestre, F. M. L. Figueiredo and C. S. R. Freire, *J. Mater. Chem. A*, 2019, **7**, 20045–20074.

60 A. R. Kim, M. Vinothkannan, K. H. Lee, J. Y. Chu, B.-H. Park, M.-K. Han and D. J. Yoo, *Int. J. Energy Res.*, 2022, **46**, 4835–4851.

61 C. Karthikeyan, Y. Sathishkumar, Y. S. Lee, A. R. Kim, D. J. Yoo and G. G. kumar, *J. Nanosci. Nanotechnol.*, 2017, **17**, 558–563.

62 A. R. Kim, J. C. Gabunada and D. J. Yoo, *Colloid Polym. Sci.*, 2018, **296**, 1891–1903.

63 L. Liu, Z. Li and Q. Che, *ACS Appl. Nano Mater.*, 2019, **2**, 2160–2168.

64 T. D. O. Gadim, F. J. A. Loureiro, C. Vilela, N. Rosero-Navarro, A. J. D. Silvestre, C. S. R. Freire and F. M. L. Figueiredo, *Electrochim. Acta*, 2017, **233**, 52–61.

65 M. M. Hasani-Sadrabadi, E. Dashtimoghadam, R. Nasseri, A. Karkhaneh, F. S. Majedi, N. Mokarram, P. Renaud and K. I. Jacob, *J. Mater. Chem. A*, 2014, **2**, 11334–11340.

66 J. Tritt-Goc, I. Jankowska, K. Pogorzelec-Glaser, R. Pankiewicz and P. Ławniczak, *Cellulose*, 2018, **25**, 281–291.

67 C. Zhan, P. R. Sharma, L. Geng, S. K. Sharma, R. Wang, R. Joshi and B. S. Hsiao, *Sci. China: Technol. Sci.*, 2019, **62**, 971–981.

68 P. R. Sharma, A. Chattopadhyay, S. K. Sharma and B. S. Hsiao, *Ind. Eng. Chem. Res.*, 2017, **56**, 13885–13893.

69 D. Wang, H. Yu, X. Fan, J. Gu, S. Ye, J. Yao and Q. Ni, *ACS Appl. Mater. Interfaces*, 2018, **10**, 20755–20766.

70 Q. Yang, T. Saito, L. A. Berglund and A. Isogai, *Nanoscale*, 2015, **7**, 17957–17963.

71 L. C. A. Barbosa, C. R. A. Maltha, A. J. Demuner, C. M. Cazal, E. L. Reis and J. L. Colodette, *BioResources*, 2013, **8**, 12.

72 S. Fujisawa, Y. Okita, H. Fukuzumi, T. Saito and A. Isogai, *Carbohydr. Polym.*, 2011, **84**, 579–583.

73 J. Zhang, H. Li and J. Zhang, *ECS Trans.*, 2019, **19**, 65–76.

74 P. Choi, N. H. Jalani and R. Datta, *J. Electrochem. Soc.*, 2005, **152**, E123.

This journal is © The Royal Society of Chemistry 2022